RSC Advances

PAPER

View Article Online
View Journal | View Issue

Cite this: *RSC Adv.*, 2017, **7**, 52702

Dual-phase spinel $Li_4Ti_5O_{12}$/anatase TiO_2 nanosheet anchored 3D reduced graphene oxide aerogel scaffolds as self-supporting electrodes for high-performance Na- and Li-ion batteries†

Ye Tian, Guobao Xu, Zelin Wu, Jianxin Zhong and Liwen Yang *

Received 23rd August 2017
Accepted 7th November 2017

DOI: 10.1039/c7ra09343h

rsc.li/rsc-advances

Self-supporting electrodes consisting of dual-phase spinel $Li_4Ti_5O_{12}$/anatase TiO_2 nanosheets and 3D reduced graphene oxide (RGO) aerogel for lithium ion batteries (LIBs) and sodium ion batteries (SIBs) were prepared *via* facile hetero-assembly, freeze-drying, mechanical compression and annealing. The 3D RGO aerogel acts as both conductive medium and self-supporting scaffold for anchored dual-phase nanosheets. The synergistic effect between the dual-phase nanosheets and the 3D highly conductive interconnected RGO network not only guarantees rapid reaction kinetics and strong structural stability of the electrodes during ion insertion/extraction, but also provides abundant accommodation for additional interfacial Li/Na storage. The self-supporting electrodes have desirable electrochemical performance such as a high reversible capacity (~200/180 mA h g^{-1} for LIB/SIB at 1C/0.1C), good rate capability (~141/117 mA h g^{-1} for LIB/SIB at 30C/10C) and superior cyclic performance (~154/101 mA h g^{-1} for LIB/SIB at 10C/6C after 1000/700 cycles). Our results have great potential in constructing self-supporting RGO electrodes embedded with anode materials for LIB and SIB applications.

1. Introduction

With ever-increasing demands in automobile and stationary energy storage applications, such as electric vehicles and renewable energy integration, considerable efforts have been devoted to developing rechargeable cost-effective energy storage devices.[1–6] Among various rechargeable energy storage systems, lithium ion batteries (LIBs) and sodium ion batteries (SIBs) are two typical energy storage devices due to their high energy densities, non-memory effect, environmentally friendly technology and long cycle life.[7,8] In particular, SIBs have great potential in smart-grid applications owing to highly abundant natural resources and the low-cost of sodium. Nevertheless, further application extensions of current LIBs and SIBs are impeded by the facts of relatively low specific capacity, inferior rate capability and poor cycle stability. Among the challenges associated with electrolytes,[9,10] separators[11,12] and electrodes[8,13] for these battery technologies, the anode material is one of the most important factor for both LIBs and SIBs in electrochemical properties and safety.[14–18] Therefore, effective material designs and preparation of reliable anodes with excellent Li/Na storage ability are critical to solve the bottleneck faced by LIBs and SIBs for their large-scale applications.

Spinel $Li_4Ti_5O_{12}$ (LTO) has been extensively investigated as a promising anode material for LIBs owing to its unique characteristics, such as "zero-strain" feature in the lattice on charging/discharging, flat operating plateau at a high potential of ~1.55 V *vs.* Li/Li^+ with a theoretical capacity of 175 mA h g^{-1} and excellent environmental benignity.[19–22] In recent years, this anode material has also been expanded to utilization in SIBs with a work potential of ~0.91 V *vs.* Na/Na^+.[23–25] The higher work voltages for LIBs and SIBs endow it with enough safety compared with traditional carbon anodes. However, its practical applications in high-performance LIBs and SIBs are hampered because of the unsatisfactory high-rate capability due to kinetic issues associated with poor electrical conductivity (*ca.* 10^{-13} S cm^{-1}) and slow ion diffusion coefficient (*ca.* 10^{-9}–10^{-13} cm^2 s^{-1} for Li^+ and 10^{-16} cm^2 s^{-1} for Na^+). To solve these problems, many effective strategies have been proposed and executed, such as reducing particle size,[7,17,26,27] aliovalent ion doping,[28–30] surface modification by secondary materials (for example, conductive carbon and carbon-free inorganic nanocrystals),[31–34] and particularly their combinations.[21,30,35–37] Among them, the integration of material engineering of nanostructured LTO and surface modification by TiO_2 in nanoscale is an effective method to augment electrochemical properties of

Hunan Key Laboratory of Micro-Nano Energy Materials and Devices, School of Physics and Optoelectronics, Xiangtan University, Hunan 411105, China. E-mail: ylwxtu@xtu.edu.cn

† Electronic supplementary information (ESI) available. See DOI: 10.1039/c7ra09343h

the LTO-based anodes. In such composites, nanostructure can shorten ion diffusion distance, while introducing TiO_2 particles will result in abundant grain boundaries to provide additional accommodation for Li/Na ions to store in the interfacial area. Wang *et al.* reported LTO nanosheets coated with rutile TiO_2 through a one-pot hydrothermal synthesis process, demonstrating higher discharge capacity and superior rate capability as LIBs anode compared to pure LTO nanosheets.[7] Wu *et al.*, reported ultrathin dual phase nanosheets consisting of alternating LTO and rutile TiO $_2$ lamellas through a facile and scalable hydrothermal method. The alternating nanoscaled lamella structure facilitates the transfer of both Li ions and electrons into spinel LTO, giving rise to an excellent cyclability with a capacity retention of 93.1% even after 500 cycles at 50C and fast rate performance with stable discharge capacities of 131.4 mA h g^{-1} at 50C.[38] Li *et al.*, prepared three-phase LTO/TiO_2 (anatase)/TiO_2 (rutile) nanoplates with high capacity of about 139 A h g^{-1} after 1000 cycles when fully charged at high current density of 4000 mA g^{-1}.[39] Nevertheless, the above-mentioned LTO/TiO_2 materials require the use of electrically insulating polymeric binder, conductive additive and metallic current collector during slurry-coating process. The traditional electrode preparation process not only increases the total cost and weight of the LIBs and SIBs, but also results in adverse effect on effective gravimetric capacity. Thus, in order to spur the applications of LTO/TiO_2 based anodes in LIBs and SIBs, designing a self-supporting electrode is highly desired. Due to its high surface area, lightweight property and highly interconnected electron pathways, three dimensional (3D) reduced graphene oxide (RGO) aerogel has been proposed as a suitable scaffolding material to anchor electroactive materials to prepare self-supporting electrodes.[40,41] Despite recent investigation on dual-phase LTO/TiO_2 materials and LTO/RGO composites, there have been few investigations on the fabrication and Li/Na storage performance of self-supporting electrode consisted of dual-phase LTO/TiO_2 nanostructures and 3D RGO aerogel.

In this work, dual-phase spinel LTO/anatase TiO_2 nanosheets anchored 3D RGO aerogel scaffold (designated as LTO-AT/RGO) was prepared as self-supporting LIB and SIB electrodes. The RGO aerogel paper acts as both conductive medium and self-supporting scaffold for dual-phase LTO-AT nanosheets. The synergistic effect between dual-phase LTO-AT nanosheets and 3D highly conductive interconnected RGO network not only guarantees rapid reaction kinetics and strong structural stability of the electrodes during ion insertion/extraction, but also provides abundant accommodations for additional interfacial Li/Na storage. The self-supporting LTO-AT/RGO electrodes have desirable electrochemical performance such as a high reversible capacity (~200/180 mA h g^{-1} for LIB/SIB at 1C/0.1C), good rate capability (~141/117 mA h g^{-1} for LIB/SIB at 30C/10C) and superior cyclic performance (~154/101 mA h g^{-1} for LIB/SIB at 10C/6C after 1000/700 cycles). Our results provide an effective method of constructing self-supporting RGO electrodes embedded with anode materials for LIB and SIB application.

2. Experimental details

2.1 Synthesis of LTO nanosheets

LTO nanosheets were fabricated by a simple way as before our reported.[31] 1.7 ml (5 mM) of tetrabutyl titanate, 0.03 g of $GdCl_3 \cdot 6H_2O$, and 0.189 g of $LiOH \cdot H_2O$ were thoroughly mixed in 20 ml of ethanol at room temperature. The solution was mixed completely with a magnetic stirrer in a closed container for 24 h and then, 25 ml of deionized water were added to the container. After stirring for 0.5 h, the solution was transferred to a 50 ml Teflon-lined stainless autoclave and placed in an oven at 180 °C for 36 h. The white powder on the bottom of the reactor was collected, washed with ethanol 3 times, and dried at 80 °C for 6 h. Finally, the white powder was heated at 700 °C for 6 h in a horizontal tube furnace in air to obtain the ultrathin LTO nanosheets.

2.2 Fabrication of the self-supporting LTO-AT/RGO aerogel

The self-supporting LTO-AT/RGO composite were fabricated *via* a hetero-assemble process, freeze-drying, mechanical compression and annealing. In a typical run, 140 mg LTO nanosheets were dispersed in the solution with 0.2 M NH_4HCO_3 under magnetic stirring for one hour to form Solution A. 60 mg GO was dissolved in deionized water to produce Solution B. Solution A was added dropwise to Solution B under fierce stirring. Flocculent GO/LTO hydrogel with uniform color and a solid-like rheological behavior was quickly produced. Subsequent washing and freeze-drying afford the formation of LTO-AT/RGO intermediate aerogel. Lastly, after mechanical compression and annealing at 600 °C, the self-supporting LTO-AT/RGO electrodes were obtained.

2.3 Materials characterization

Powder X-ray diffraction (XRD) with a copper Kα radiation source (λ = 0.154 nm) was performed to identify the crystal structures of RGO and self-supporting LTO-AT/RGO. The scanning electron microscopy (SEM, JEOL, JSM-6490) and transmission electron microscopy (TEM, JEOL 2100) were used to characterize morphologies and microstructures of the samples. X-ray photoelectron spectroscopy (XPS) with an Al Kα source (Kratos Analytical Ltd., UK) was carried out and calibrated by using C 1s peak with the binding energy of 284.8 eV. Nitrogen adsorption–desorption isotherm measurements of the samples were conducted at 77 K (Quantachrome NOVA 4000e). Raman spectra were obtained on a Renishaw inVia system with a laser excitation source operating at λ = 532 nm. Thermal gravimetric analysis (TGA) and differential scanning calorimetry (DSC) were performed using a TGA 2050 thermogravimetric analyzer. Fourier transform infrared (FTIR) spectra were measured on a FTS-3000 Fourier transform infrared spectrophotometer.

2.4 Electrochemical characterization

The electrochemical tests were performed on two-electrode CR2032-type coin cells. The self-supporting LTO-AT/RGO composites were directly used as the working electrodes in the

lithium and sodium cells. The assembly of coin cells were conducted in an glove box with filled argon using Na/Li foils as counter electrodes, 1 M $NaClO_4$ in ethylene carbonate (EC)/propylene carbonate (PC) with volume ratio of 1 : 1 and 1 M $LiPF_6$ in a 1 : 1 (v/v) mixture of ethylene carbonate/dimethyl carbonate as electrolyte, the glass fibre (Whatman GF/D) and Celgard 2400 Polypropylene as separators for the sodium and lithium cells, respectively. Cyclic voltammetry (CV) was measured on a CHI660E electrochemical workstation. Galvanostatic charge–discharge (GCD) measurements were carried out at various current densities on multi-channel battery test system (NEWARE BTS-610). Electrochemical impedance spectroscopy (EIS) measurements were conducted on an electrochemical workstation (CHI660D) with the frequency range from 0.01 to 100 kHz.

3. Results and discussion

3.1 Material preparation and characterization

Fig. 1 illustrates the overall fabrication process of self-supporting LTO-AT/RGO electrodes, including hetero-assembly of GO and LTO nanosheets, freeze-drying, mechanical compression and annealing. In our previous studies,[32] LTO nanosheets prepared by hydrothermal method followed by calcinations have abundant charged ions on the surface in the solution with high ionic strength containing 0.2 M NH_4HCO_3, and a fine colloid of the LTO nanosheets is readily obtained. When the GO nanosheets with negative charges and the LTO nanosheets in the solution with high ionic strength are mixed, hetero-assembly between GO and LTO nanosheets accompanying spontaneous co-precipitation occurs. As a result, flocculent GO/LTO hydrogel with uniform color and a solid-like rheological behavior was quickly produced. Subsequent washing and freeze-drying afford the formation of LTO-AT/RGO intermediate aerogel, which can be plastically deformed *via* mechanical compression to form self-supporting intermediate. During this process, a certain amount of Li in LTO nanosheets was washed away, depending on the time of water washing. The deficiency of Li plays a key role in the formation of dual-phase LTO-AT nanosheets in the following thermal treatment.[7] After annealing at 600 °C, the self-supporting LTO-AT/RGO electrodes are obtained accompanying reduction of GO to RGO and complete decomposition of the remaining NH_4HCO_3. As shown in Fig. 2a and b, the self-supporting LTO-AT/RGO electrodes are

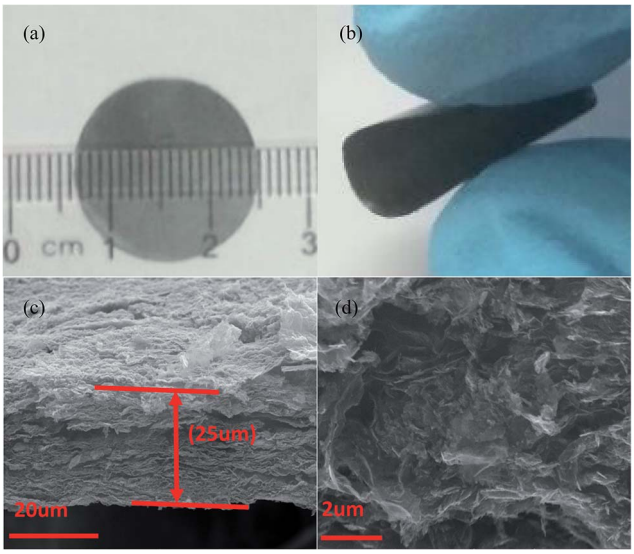

Fig. 2 (a and b) Optical image of the self-supporting LTO-AT/RGO electrodes; (c and d) cross-sectional SEM image of the self-supporting LTO-AT/RGO electrodes.

mechanically robust with excellent flexibility (even sustaining 180° bending). The excellent mechanical properties suggest direct use for LIB and SIB electrodes without any binders.

Fig. 2c depicts the cross-sectional SEM image of the self-supporting LTO-AT/RGO electrodes with a thickness of about 25 μm, disclosing a layered feature and good thickness uniformity. The high-magnification SEM image (Fig. 2d) reveals that the anchored LTO-AT nanosheets are well distributed within interconnected RGO networks. The results confirm that during hetero-assembly and spontaneous co-precipitation of LTO nanosheets and GO, the former with positive ions prefer to settle at the functional group sites on the surface and at the periphery of the latter. Fig. 3a shows the TEM image of LTO nanosheets with clear surface and large size. Meanwhile, the TEM images of LTO-AT/RGO electrode are shown in Fig. 3b and c, in which the LTO nanosheets with small nanosheets on the surface are tightly anchored on the RGO sheets. Further HRTEM observation of the marked region in Fig. 3c (see Fig. 3d) indicates that characteristic (101) lattice plane of anatase TiO_2 with a lattice spacing of 0.35 nm and (111) one of spinel LTO with a spacing of 0.48 nm can be distinguished. The results reveal that these nanosheets are composed of spinel LTO and anatase

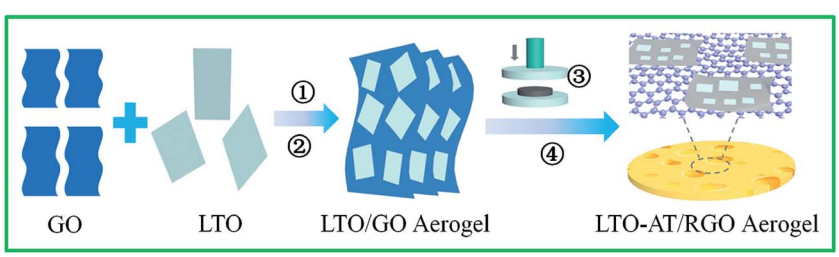

Fig. 1 Schematic of the fabrication procedures of monolithic LTO-AT/RGO aerogel. Herein, ①, ②, ③ and ④ represent hetero-assembly, washing and freeze-drying, mechanical compression and annealing, respectively.

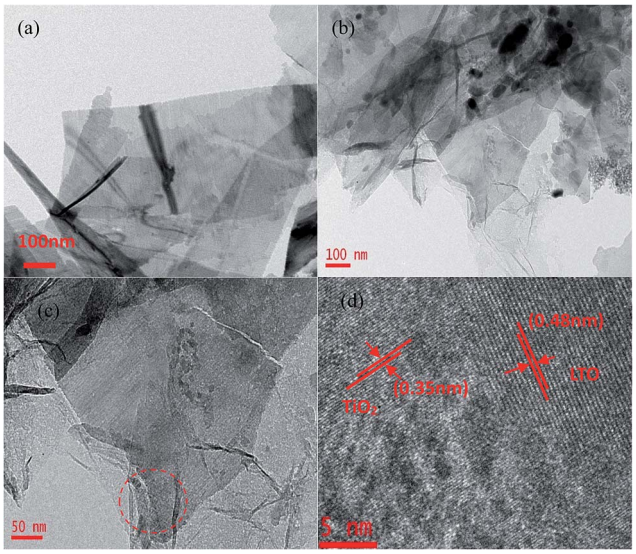

Fig. 3 (a) TEM image of the LTO nanosheets; (b) and (c) TEM images at low and high magnification, respectively; (d) HRTEM image acquired from the region marked by dot circle in (c).

TiO_2. The crystal structure of the LTO-AT/RGO electrodes is further characterized by XRD. As shown in Fig. 4a, besides LTO (JCPDS no. 49-0207),[42] anatase TiO_2 (JCPDS card no. 21-1272)[33] was also detected in the sample, in which the most intensity of the XRD peaks of LTO at 18.4 degrees in sample may be ascribed to the preferential orientation of the (111) planes. While the samples have been obtained in different time of the water washing and characterized by XRD. As shown in Fig. S1,† the ratio of the most intensity peak of the LTO (111) *vs.* AT (101) is 1.12, 1.33, 1.4 and 1.6 at 48 h, 24 h, 12 h and 6 h, respectively. These results indicated that the change of ratio is not obvious with the time of washing. In general, the intensity of XRD peaks from one crystalline phase in a multiphase composite depends on the weight fraction of the corresponding phase in the composite. Thus, the weight fraction of anatase TiO_2 can be calculated by measuring the intensities of (101) peak of anatase TiO_2 and (111) peak of LTO.[38] Accordingly, the weight fraction of the anatase TiO_2 in the prepared LTO-AT/RGO aerogel paper was measured to be around 0.4. No XRD peak located at 12.4° from GO is observed, suggesting that GO has been reduced to RGO *via* thermal treatment at 600 °C. The should peak at 26° ascribed to characteristic (002) interlayer diffraction of few-layer RGO nanosheets is weak, suggesting that the RGO sheets are effectively separated without serious self-stacking by the anchored LTO-AT nanosheets.

Fig. 4b displays the Raman spectra of the as-prepared LTO-AT/RGO electrodes and reference samples. The Raman bands at 230, 432 and 687 cm^{-1} are attributed to characteristic vibration modes in cubic spinel LTO, associated with the vibration (F_{2g}) of lithium which is octahedrally-coordinated by oxygen, stretching vibration of Li–O ionic bonds located in the LiO_4 tetrahedra (E_g) and stretching vibration of Ti–O covalent bonding in TiO_6 octahedra, respectively. The Raman bands located at 149, 396.8, 511.9 and 638.8 cm^{-1} can be assigned to the E_g, B_{1g}, A_{1g} and E_g modes of anatase TiO_2,[36] respectively. Besides these Raman modes from spinel LTO and anatase phase TiO_2, two strong peaks, denoted as the disorder peak (D, centered at 1350 cm^{-1}) and graphitic peak (G, at 1594 cm^{-1}) are also observed from as-prepared LTO-AT/RGO electrodes, suggesting that LTO-AT nanosheets are highly dispersed into surrounding RGO matrix. Compared with peak intensity ratio for the D and G bands (I_D/I_G = 1.03) of the referenced RGO sample, the ratio of the LTO-AT/RGO electrodes increase to 1.09, indicating strong electronic coupling between LTO-AT nanosheets and RGO, leading to effective electron transport of the overall electrode during electrochemical processes. Fig. 4c shows FTIR spectra of the as-prepared LTO-AT/RGO electrodes and reference samples. The peaks at 450–900 cm^{-1} can be attributed to the Ti–O–Ti stretching vibration modes in spinel LTO and anatase TiO_2. The intensity of the peak at 1626 cm^{-1} decreases notably and a new peak at 1564 cm^{-1} appears reflecting the skeletal vibration of RGO sheets, indicates effective elimination of carboxyl and epoxy functional groups and the transformation of GO to RGO.[43] The Raman and FTIR spectra confirm that the LTO-AT/RGO electrodes *via* above-mentioned fabrication contains RGO matrix with highly dispersed LTO-AT nanosheets, which is consistent with the XRD results. The surface chemical composition and electronic states of the LTO-AT/RGO electrodes are determined by XPS. The survey XPS spectrum and high-resolution Li 1s, Ti 2p, O 1s, C 1s and N 1s spectra (see Fig. 4d) reveal the presence of Li, Ti, O, C and N. Fig. 4e shows high-resolution XPS spectrum of Ti 2p, revealing two characteristic peaks at 458.7 and 464.5 eV assigned to Ti $2p_{3/2}$ and $2p_{1/2}$, respectively, from titanium in the IV oxidation state. Compared with those from the referenced LTO nanosheets, the binding energy of Ti 2p from the LTO-AT/RGO electrode shifts toward high-energy direction, suggesting strong electron interaction between the LTO-AT nanosheets and surrounding RGO matrix. In addition, TGA/DSC results (see Fig. 4f) shows that the LTO-AT/RGO electrode is composed of ~62 wt% LTO-AT nanosheets.

3.2 Electrochemical performance in sodium ion batteries

The Na storage ability of the LTO-AT/RGO electrode is firstly investigated. Fig. 5a shows the CV curve at a scanning rate of 0.2 mV s^{-1} in the potential range between 2.5 and 0.3 V *vs.* Na^+/Na, demonstrating the CV trace in the first cycle is different from those of the subsequent ones, suggesting possible existence of structural deformation and reconstruction induced by electrochemical atomic rearrangements around the LTO-AT nanosheets due to the formation of SEI layers. Previous studies reveals that the redox peaks assigned to Na^+ insertion/extraction in anatase TiO_2 were located at about 0.76 and 0.83 V, which overlap those representing Na^+ insertion/extraction in the LTO crystal lattice according to the following three-phase separation mechanism: $2Li_4Ti_5O_{12} + 6Na^+ + 6e \rightarrow Li_7Ti_5O_{12} + LiNa_6Ti_5O_{12}$.[34,44] Therefore, the couple of redox peaks located at ~0.63 V (cathodic peak) and ~1.06 V (anodic peak) *vs.* Na^+/Na observed in the subsequent cycles include the contribution from reversible insertion/extraction of sodium in

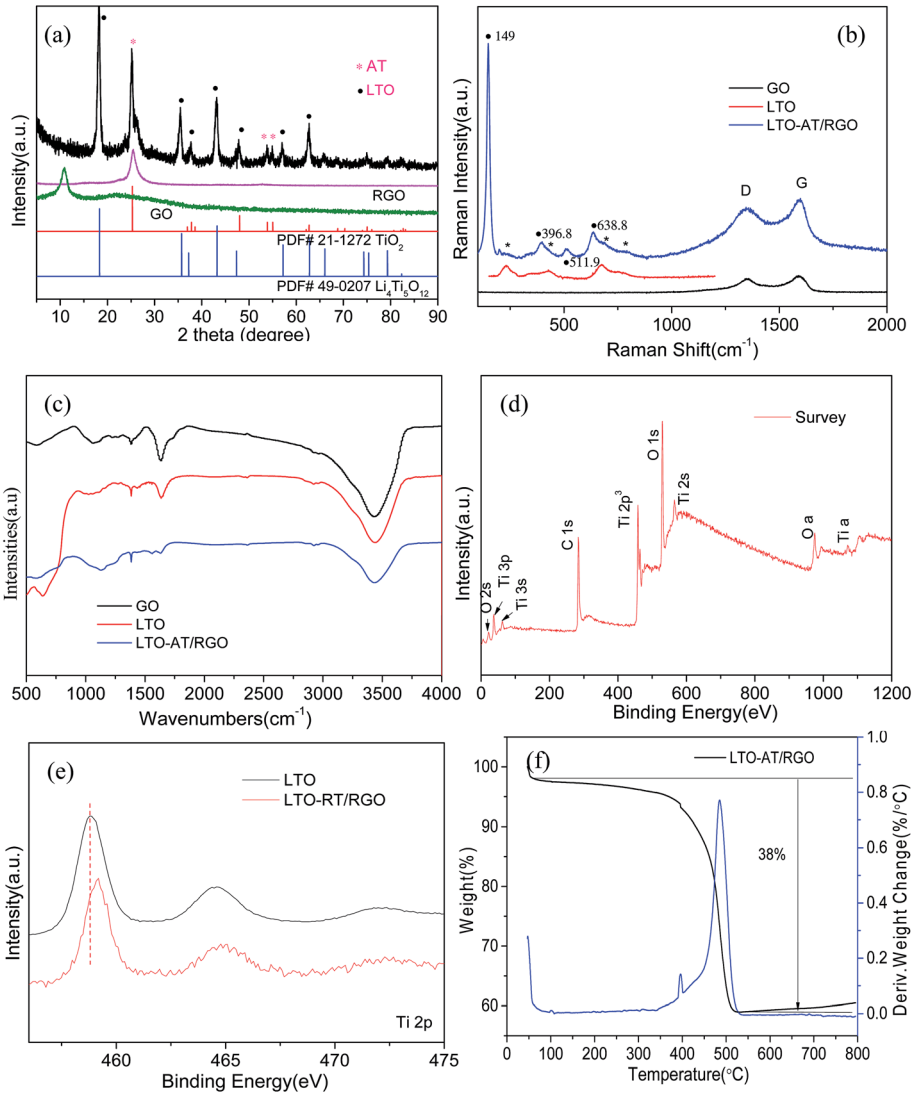

Fig. 4 (a) XRD patterns of the self-supporting LTO-AT/RGO aerogel and referenced samples; (b and c) Raman spectra and FTIR spectra of the self-supporting LTO-AT/RGO aerogel and referenced samples; (d) survey XPS spectrum of self-supporting LTO-AT/RGO aerogel; (e) high-resolution Ti XPS spectra of the self-supporting LTO-AT/RGO aerogel and referenced LTO nanosheets; (f) TGA/DSC data of the self-supporting LTO-AT/RGO aerogel.

both LTO and anatase TiO_2. The redox peak positions are almost invariable during successive scans, implying superior cycling stability of the LTO-AT/RGO electrode. In addition, another couple of weak redox peaks at 1.65 V (anodic peak) and 1.24 V (cathodic peak) can be observed. Since they cannot be attributed to Na^+ insertion/extraction into anatase TiO_2 and LTO, this pair of redox peaks likely originates from Na^+ storage at interfaces of LTO/anatase TiO_2, LTO/RGO and anatase TiO_2/RGO. Fig. 5b shows the typical discharging/charging profiles of the LTO-AT/RGO electrode at a current rate of 0.5C, demonstrating initial discharge and charge capacities are 217 and 190 mA h g^{-1}, respectively. The Na^+ insertion process includes three domains with a sloping region (I) from open circuit voltage to ~1.02 V, plateau (II) about 0.75 V, and another sloping region (III) from ~0.65 to 0.3 V. Domains I and II represents Na^+ insertion into the LTO and anatase TiO_2, while Domain III originates from Na^+ storage at the LTO/anatase TiO_2, LTO/RGO and anatase TiO_2/RGO interfaces.

The inset in Fig. 5c is the charging–discharging profiles at different current densities, demonstrating apparent decrease in the voltage plateau region while no obvious change in the sloping region with increasing current density. The results indicate that at high rates, Na^+intercalation into the LTO and anatase TiO_2 becomes difficult, whereas interfacial Na storage is still sufficient. The LTO-AT/RGO electrodes deliver reversible capacities of 184, 178, 167, 150, 139 and 117 mA h g^{-1} at rates of 0.5, 1, 2, 4, 6 and 10C respectively. Even at a high rate of 20C, a reversible capacity of 77 mA h g^{-1} is maintained. When the current rate is recovered to 0.5C after cycling at various rates, the capacity can recover to 171 mA h g^{-1}. These results demonstrate superior rate capability of the LTO-AT/RGO electrode. Furthermore, the cycling durability is tested at a large

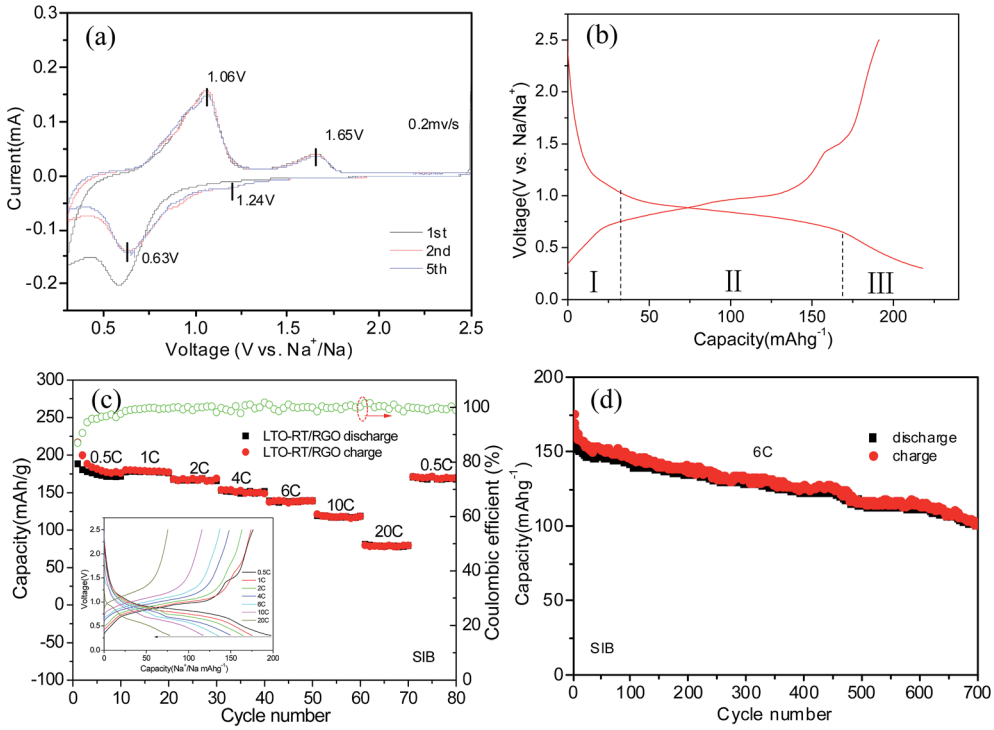

Fig. 5 (a) Typical CVs of the self-supporting LTO-AT/RGO electrode for SIBs at scan rate 0.2 mV s^{-1}; (b) typical charge–discharge profiles of the self-supporting LTO-AT/RGO electrode at 0.5C; (c) rate performance, coulombic efficient and charge–discharge profiles (see inset) of the self-supporting LTO-AT/RGO electrode; (d) cycling performance of the self-supporting LTO-AT/RGO electrode for SIBs at 6C.

current density of 6C. As shown in Fig. 4d, after a quick decay in the initial 10 cycles, the LTO-AT/RGO electrode delivers a high capacity of 158 mA h g^{-1} with a coulombic efficiency approaching 100%. A capacity of 101 mA h g^{-1} is maintained after 700 cycles with a capacity loss of 0.067 per cycle, confirming excellent long-term cycling sustainability of the LTO-AT/RGO electrode.

To gain insight into the superior electrochemical performance of the LTO-AT/RGO electrode, EIS measurements were performed after the rate capability test. The obtained Nyquist plots (see Fig. 6a) include mainly a semicircle related to charge-transfer impedance (R_{ct}) on electrode–electrolyte interface in high frequency, and an incline straight line attributed to Warburg impedance (Z_w) in low frequency region. Using the inset equivalent circuit model, the calculated R_{ct} value for the LTO-AT/RGO electrode is 88.35 (see Table 1). The Na^+ chemical diffusion coefficient (DNa) is also calculated according to the following equations:

$$D_{Na} = \frac{R^2T^2}{2A^2n^4F^4C^2\sigma^2} \quad (1)$$

$$Z = R_s + R_{ct} + \sigma\omega^{-1/2} \quad (2)$$

where R, T, A, n, F, C and σ are the gas constant, absolute temperature, surface area of the electrode, number of electrons transferred in the half reaction of the redox couple, Faraday's constant, Na^+ concentration, and Warburg factor, respectively. The value of σ can be obtained (Table 1) from the slope of the lines between Z' and $\omega^{-1/2}$ (see the inset of Fig. 6a). The calculated DNa value of the LTO-AT/RGO electrode is 7.5×10^{-15} (see Table 1). The small Rct and large DNa in the LTO-AT/RGO electrode indicate effective charge transfer process at the electrode/electrolyte interface and rapid electrochemical kinetics due to increased grain boundary density which had a lower energy barrier for Na diffusion and in fact facilitated Na ion diffusion. Furthermore, we performed kinetic analysis based on CV results that has been proven as a powerful technique for studying electrochemical kinetics of electrode materials toward Na^+. The inset of Fig. 6b shows the CV curves of the LTO-AT/RGO electrode at different scan rates. In general, the currents (i) responding to the sweeping rates (v) in the CV curves follow the equation of $i = av^b$, where a and b are adjustable values.[45,46] If $b = 1$, it suggests that the total charge (Q) originates from the capacitive process (interfacial Na storage process) and if $b = 0.5$, it is totally diffusion-controlled (Na^+ insertion/extraction process). Fig. 5b shows the log(v)–log(i) plots for the LTO-AT/RGO electrode and the fitted b values for the cathodic and anodic peak currents are 0.872 and 0.837, respectively, implying that that the charge (thus the capacity) comes from two contributions. According to the equation of $i = k_1v + k_2v^{\frac{1}{2}}$,[47] the capacitive (interfacial) contribution can be separated, where k_1v and $k_2v^{1/2}$ represent the contributions from the capacitive (interfacial Na storage process) charge and diffusion-controlled (Na^+ insertion/extraction process) one, respectively. For example, as shown in Fig. 5c, the interfacial capacitive contribution at 0.5 mV s^{-1} is determined to be 50.1%

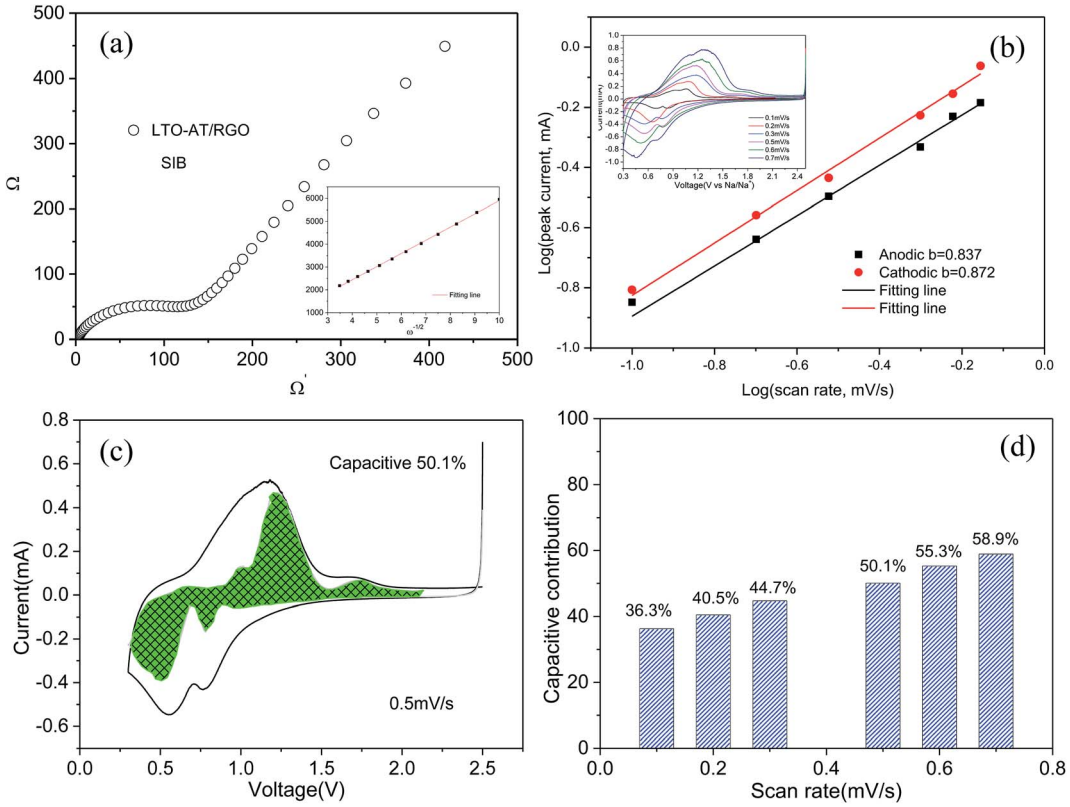

Fig. 6 (a) EIS spectra of self-supporting LTO-AT/RGO electrode and referenced one for SIBs; (b) CV curves at various scan rates of self-supporting LTO-AT/RGO electrode for SIBs (see inset) and calculating the *b*-value according to log(*i*)–log(*v*) plots; (c) typical CV curve with the contribution from capacitive effect shown by the highlighted region at 0.5 mV s^{-1}; (d) comparison of the capacitive charge contributions at different scan rates.

Table 1 The calculated R_{ct} and R_s values for the LTO-AT/RGO electrodes according to EIS results in Fig. 5 and 6

Compound	Half-cells	R_s (Ω)	R_{ct} (Ω)	D (cm^2 s^{-1})
LTO-AT/RGO	Lithium-ion battery	3.21	75.85	2.1×10^{-12}
	Sodium-ion battery	6.51	88.35	7.5×10^{-15}

in the LTO-AT/RGO electrode. With the scanning rates being increased from 0.1 to 0.7 mV s^{-1} (see Fig. 6d), the interfacial capacitive contributions increase from 36.3% to 58.9%. The results indicate that the kinetics of Na^+ intercalation process becomes limited at high rates but the kinetics of interfacial Na storage is still sufficient in the LTO-AT/RGO electrode, which is consistent with the aforementioned sodium storage performance observed at various current densities. The CV kinetic analysis disclose that the intercalation-based and interfacial Na storage behaviors take effect simultaneously, and particularly the latter keeps highly efficient at high rates in the LTO-AT/RGO electrode, which endows it with excellent Na storage performance.

3.3 Electrochemical performance in lithium ion batteries

Considering great advantage and application of LTO-based anodes in high-performance LIBs, we also examine Li storage performance of the LTO-AT/RGO electrode. Fig. 7a shows the CV curves of initial five cycles for as-prepared electrodes between 1 and 2.5 V (*vs.* Li/Li^+) with a scan rate of 0.2 mV s^{-1}.

Two pairs of oxidation and reduction peaks at 2.08 V/1.68 V and 1.68 V/1.44 V, which are ascribed to anatase TiO_2 and spinel LTO, respectively, indicating the feature of a dual phase composite material. The redox peak positions are unchanged during successive scans demonstrating excellent reversibility of the LTO-AT/RGO electrode. The initial discharge profiles for the LTO-AT/RGO electrode with a current rate of 2C are shown in Fig. 7b. The flat discharge plateau at about 1.55 V due to Li ions being extracted from the spinel LTO and the voltage one at around 1.7 V verified the lithium ion insertion of anatase TiO_2 can be observed, which are in agreement with the CV results. Similarly, the Li^+ insertion process can be divided into five domains (see inset of Fig. 7b) with a sloping region (I) from open circuit voltage to ~1.7 V, plateau (II) about 1.7 V, a sloping region (III) from ~1.7 to 1.55 V, plateau (IV) about 1.55 V and another sloping region (V) from 1.55 to 1 V. Domains I, III and IV originate from Li insertion into anatase TiO_2 and spinel LTO, while domain II and V associates with Na storage at the interface of LTO/anatase TiO_2, LTO/RGO and anatase TiO_2/RGO. The charge–discharge profiles acquired at different current densities from 1 to 100C (see inset of Fig. 7c) of LTO-AT/RGO electrode show similar feature that the voltage plateaus decrease

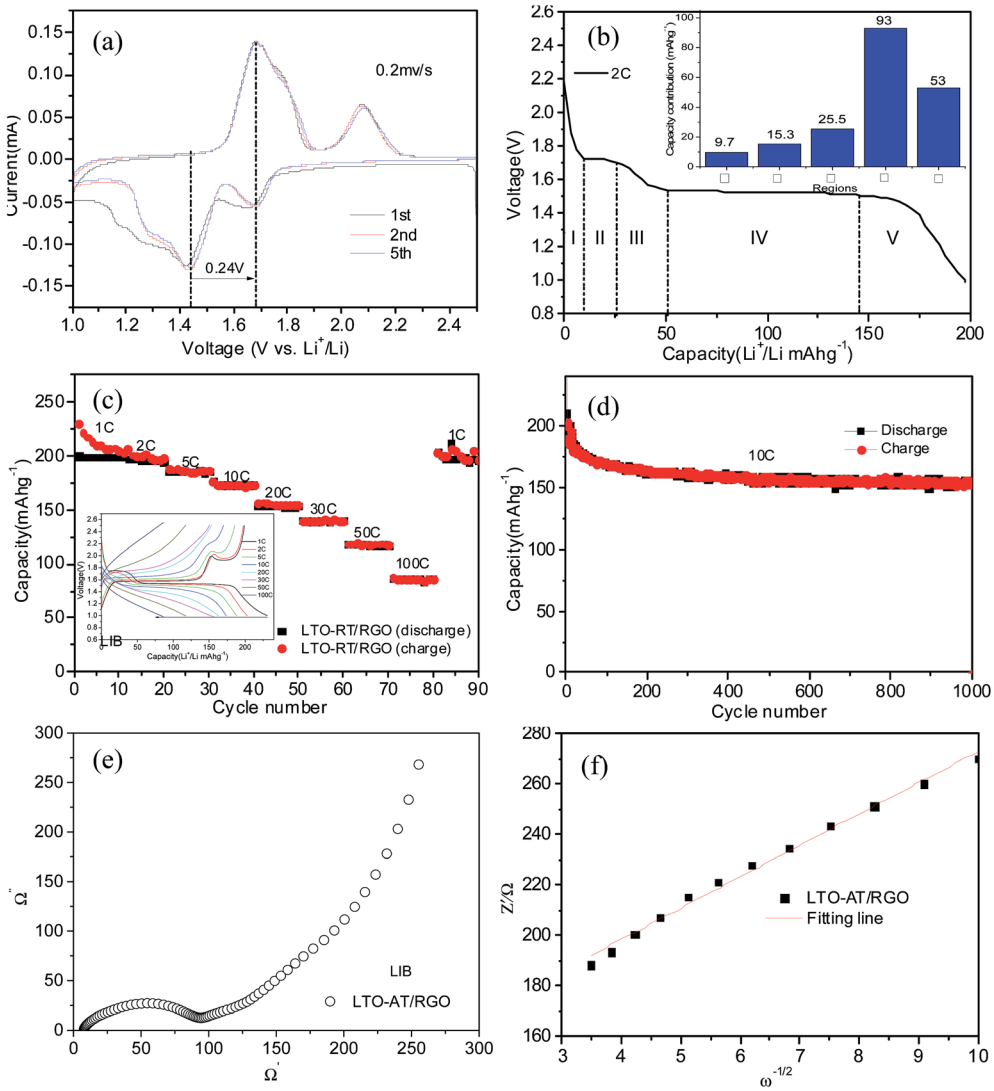

Fig. 7 (a) CVs of the self-supporting LTO-AT/RGO electrode for LIBs at scan rate of 0.2 mV s^{-1}; (b) typical discharge profiles of the self-supporting LTO-AT/RGO electrode at 2C; (c) rate capacity and charge–discharge curves (see inset) of the LTO-AT/RGO electrode for LIBs; (d) cycling performance of the self-supporting LTO-AT/RGO electrode at 10C; (e) Nyquist plots of the self-supporting LTO-AT/RGO electrode for LIBs; (f) corresponding Z' plots against $\omega^{-1/2}$ plots against at the low frequency region (10–0.1 Hz).

apparently while the sloping region is almost unchanged at high current densities, revealing that interfacial Li storage is more sufficient than that associated with Li^+ intercalation into LTO and anatase TiO_2. The corresponding rate performance (see Fig. 7c) shows high and stable capacity. At rates of 1, 2, 5, 10, 20, 30 and 50C, the LTO-AT/RGO electrode delivers discharge capacities of 208, 197, 186, 173, 154, 138 and 115 mA h g^{-1}, respectively. Even at 100C, a reversible capacity of 86 mA h g^{-1} is maintained implying rapid charging and discharging within a few minutes for high energy and power densities. When the rate is returned to 1C after high-rate cycling, a high capacity of 202 mA h g^{-1} in subsequent cycling can be recovered, suggesting good structural integrity of the prepared electrode. Fig. 7d displays the long-term cycling performance of the LTO-AT/RGO electrode at a high current density of 10C, demonstrating a stable capacity of 173 mA h g^{-1} with the coulombic efficiency approaching 100% after 50 cycles. A capacity of 154 mA h g^{-1} is still retained after 1000 cycles with a capacity loss of only 19 mA h g^{-1}. The Fig. S3a and b† show morphology of the as-cycled LTO-AT/RGO electrode with no apparent difference comparing the before-cycled SEM images and RGO sheets are in good contact with LTO-AT nanosheets. The crystalline structure is also tested *via* Raman scattering. As shown in Fig. S4,† besides the strong Raman peaks from RGO, the characteristic peaks at 230, 432 and 687 cm^{-1} are ascribed to characteristic vibration modes in cubic spinel LTO and 149, 396.8. 511.9 and 638.8 cm^{-1} can be assigned to the E_g, B_{1g}, A_{1g} and E_g modes of anatase TiO_2. The results show that the LTO-AT/RGO electrode is robust and can sustain long-term cycling. In a word, the high-rate and long-term cycling performance of the LTO-AT/RGO electrode are excellent, compared to the results reported in LTO-based LIB anodes using traditional

slurry-coating process.[21,23,25,26,48] In addition, EIS measurements (see Fig. 6e and f) with the simulated results (see Table 1) reveal that the LTO-AT/RGO electrode has low charge-transfer resistance and large Li ion diffusion coefficient. The CV curves of the LTO-AT/RGO electrode material as lithium-ion battery at different scan rates have been also studied (Fig. S2†). Although, compared LTO-AT/RGO electrode in sodium ion battery, the capacitive contribution and *b* value are smaller in lithium ion battery, which may be attributed to the anatase TiO2 with understanding diffusion-controlled processes as electrode in lithium ion batteries and larger interfacial contribution in sodium ion batteries.[49] These results indicate that the kinetics for the Li^+ intercalation process is limited at high rates, whereas the kinetics for the interfacial Li storage process is still sufficient. In brief, the results demonstrate that the LTO-AT/RGO anode is suitable for high-performance LIBs.

4. Conclusion

Self-supporting LTO-AT/RGO electrode was successfully prepared *via* a facile hetero-assembly, freeze-drying, mechanical compression and annealing. Such composite was directly utilized as anodes for LIBs and SIBs without any additives. The synergistic effect between dual-phase LTO-AT nanosheets and 3D highly conductive interconnected RGO network not only guarantee rapid reaction kinetics and strong structural stability of the electrodes during ion insertion/extraction, but also provide abundant accommodation sites for efficient interfacial Li/Na storage. For SIBs, the self-supporting LTO-AT/RGO anode have desirable electrochemical performance such as a high capacity (~208 mA h g^{-1} at 0.1C), good rate capability (~~141/117 at 30C/10C) and superior cyclic performance (~101 at 6C after 700 cycles). As anodes for LIBs, it demonstrates high-rate performance with a capacity of 86 mA h g^{-1} at 100C and long-term cycling performance with a capacity of 154 mA h g^{-1} after 1000 cycles at 10C. Our results are important for future research in additive-free electrode fabrication as the fabrication technique is facile and can be extended for anchoring other materials on 3D RGO scaffold material to constructing self-supporting anode for LIB and SIB applications.

Conflicts of interest

There are no conflicts to declare.

Acknowledgements

This work was financially supported by the Grants from National Natural Science Foundation of China (No. 11474242 and 51472209), the Research Foundation of Education Bureau of Hunan Province, China (Grant No. 15B237) and the Hunan Provincial Innovation Foundation for Graduate (No. CX2016B254).

References

1 P. Simon and Y. Gogotsi, *Nat. Mater.*, 2008, **7**, 845–854.
2 S. Evers and L. F. Nazar, *Acc. Chem. Res.*, 2012, **46**, 1135–1143.
3 N. Yabuuchi, K. Kubota, M. Dahbi and S. Komaba, *Chem. Rev.*, 2014, **114**, 11636–11682.
4 X. Wang, X. Lu, B. Liu, D. Chen, Y. Tong and G. Shen, *Adv. Mater.*, 2014, **26**, 4763–4782.
5 J. B. Goodenough and Y. Kim, *Chem. Mater.*, 2009, **22**, 587–603.
6 M. Armand and J.-M. Tarascon, *Nature*, 2008, **451**, 652–657.
7 Y.-Q. Wang, L. Gu, Y.-G. Guo, H. Li, X.-Q. He, S. Tsukimoto, Y. Ikuhara and L.-J. Wan, *J. Am. Chem. Soc.*, 2012, **134**, 7874–7879.
8 D. Xie, X. Xia, Y. Zhong, Y. Wang, D. Wang, X. Wang and J. Tu, *Adv. Energy Mater.*, 2017, **7**, 1601804.
9 Z. Zhang, L. Hu, H. Wu, W. Weng, M. Koh, P. C. Redfern, L. A. Curtiss and K. Amine, *Energy Environ. Sci.*, 2013, **6**, 1806–1810.
10 J. Feng, Z. Zhang, L. Li, J. Yang, S. Xiong and Y. Qian, *J. Power Sources*, 2015, **284**, 222–226.
11 S. Wei, S. Choudhury, J. Xu, P. Nath, Z. Tu and L. A. Archer, *Adv. Mater.*, 2017, **29**, 1605512.
12 Y.-E. Miao, G.-N. Zhu, H. Hou, Y.-Y. Xia and T. Liu, *J. Power Sources*, 2013, **226**, 82–86.
13 M. Moradi, Z. Li, J. Qi, W. Xing, K. Xiang, Y.-M. Chiang and A. M. Belcher, *Nano Lett.*, 2015, **15**, 2917–2921.
14 B. Qu, C. Ma, G. Ji, C. Xu, J. Xu, Y. S. Meng, T. Wang and J. Y. Lee, *Adv. Mater.*, 2014, **26**, 3854–3859.
15 J. Chang, X. Huang, G. Zhou, S. Cui, P. B. Hallac, J. Jiang, P. T. Hurley and J. Chen, *Adv. Mater.*, 2014, **26**, 758–764.
16 L. Gao, L. Wang, S. Dai, M. Cao, Z. Zhong, Y. Shen and M. Wang, *J. Power Sources*, 2017, **344**, 223–232.
17 X. Jia, Y. Lu and F. Wei, *Nano Res.*, 2016, **9**, 230–239.
18 G. Hu, P. Chen, Z. Liu, Y. Cao, Z. Zhang, Z. Peng and D. Ke, *J. Alloys Compd.*, 2017, **696**, 177–184.
19 S. Chen, Y. Xin, Y. Zhou, Y. Ma, H. Zhou and L. Qi, *Energy Environ. Sci.*, 2014, **7**, 1924–1930.
20 A. K. Haridas, C. S. Sharma and T. N. Rao, *Small*, 2015, **11**, 290–294.
21 E. F. Rodriguez, F. Xia, D. Chen, A. F. Hollenkamp and R. A. Caruso, *J. Mater. Chem. A*, 2016, **4**, 7772–7780.
22 K. Qian, L. Tang, M. Wagemaker, Y. B. He, D. Liu, H. Li, R. Shi, B. Li and F. Kang, *Adv. Sci.*, 2017, 1700205.
23 L. Y. Yang, H. Z. Li, J. Liu, S. S. Tang, Y. K. Lu, S. Te Li, J. Min, N. Yan and M. Lei, *J. Mater. Chem. A*, 2015, **3**, 24446–24452.
24 C. Chen, H. Xu, T. Zhou, Z. Guo, L. Chen, M. Yan, L. Mai, P. Hu, S. Cheng and Y. Huang, *Adv. Energy Mater.*, 2016, **6**, 1600322.
25 X. Feng, H. Zou, H. Xiang, X. Guo, T. Zhou, Y. Wu, W. Xu, P. Yan, C. Wang and J.-G. Zhang, *ACS Appl. Mater. Interfaces*, 2016, **8**, 16718–16726.
26 W. Liu, D. Shao, G. Luo, Q. Gao, G. Yan, J. He, D. Chen, X. Yu and Y. Fang, *Electrochim. Acta*, 2014, **133**, 578–582.
27 H. Park, T. Song, H. Han and U. Paik, *J. Power Sources*, 2013, **244**, 726–730.
28 J. G. Kim, M. S. Park, S. M. Hwang, Y. U. Heo, T. Liao, Z. Sun, J. H. Park, K. J. Kim, G. Jeong and Y. J. Kim, *ChemSusChem*, 2014, **7**, 1451–1457.

29 T.-F. Yi, Y. Xie, L.-J. Jiang, J. Shu, C.-B. Yue, A.-N. Zhou and M.-F. Ye, *RSC Adv.*, 2012, **2**, 3541–3547.
30 Y. Ma, B. Ding, G. Ji and J. Y. Lee, *ACS Nano*, 2013, **7**, 10870–10878.
31 G. Xu, W. Li, L. Yang, X. Wei, J. Ding, J. Zhong and P. K. Chu, *J. Power Sources*, 2015, **276**, 247–254.
32 Z. Yang, Q. Meng, Z. Guo, X. Yu, T. Guo and R. Zeng, *Energy*, 2013, **55**, 925–932.
33 L. Gao, D. Huang, Y. Shen and M. Wang, *J. Mater. Chem. A*, 2015, **3**, 23570–23576.
34 L. Gao, L. Wang, S. Dai, M. Cao, Z. Zhong, Y. Shen and M. Wang, *J. Power Sources*, 2017, **344**, 223–232.
35 B. Zhang, Y. Yu, Y. Liu, Z.-D. Huang, Y.-B. He and J.-K. Kim, *Nanoscale*, 2013, **5**, 2100–2106.
36 J.-Y. Liao, V. Chabot, M. Gu, C. Wang, X. Xiao and Z. Chen, *Nano Energy*, 2014, **9**, 383–391.
37 K.-T. Kim, C.-Y. Yu, C. S. Yoon, S.-J. Kim, Y.-K. Sun and S.-T. Myung, *Nano Energy*, 2015, **12**, 725–734.
38 L. Wu, X. Leng, Y. Liu, S. Wei, C. Li, G. Wang, J. Lian, Q. Jiang, A. Nie and T. Y. Zhang, *ACS Appl. Mater. Interfaces*, 2017, **9**, 4649–4657.
39 S. Wang, Y. Yang, W. Quan, Y. Hong, Z. Zhang, Z. Tang and J. Li, *Nano Energy*, 2017, **32**, 294–301.
40 Y. Jiao, H. Zhang, T. Dong, P. Shen, Y. Cai, H. Zhang and S. Zhang, *J. Mater. Sci.*, 2017, **52**, 3233–3243.
41 M. Xu, L. Wang, X. Zhao, J. Song, H. Xie, Y. Lu and J. B. Goodenough, *Phys. Chem. Chem. Phys.*, 2013, **15**, 13032–13037.
42 C. Chen, Y. Huang, C. An, H. Zhang, Y. Wang, L. Jiao and H. Yuan, *ChemSusChem*, 2015, **8**, 114–122.
43 S. Yu, L. Yang, Y. Tian, P. Yang, F. Jiang, S. Hu, X. Wei and J. Zhong, *J. Mater. Chem. A*, 2013, **1**, 12750–12758.
44 G. Hasegawa, K. Kanamori, T. Kiyomura, H. Kurata, K. Nakanishi and T. Abe, *Adv. Energy Mater.*, 2015, **5**, 1400730.
45 B. Wang, X. Li, B. Luo, L. Hao, M. Zhou, X. Zhang, Z. Fan and L. Zhi, *Adv. Mater.*, 2015, **27**, 1526–1532.
46 V. Augustyn, J. Come, M. A. Lowe, J. W. Kim, P.-L. Taberna, S. H. Tolbert, H. D. Abruña, P. Simon and B. Dunn, *Nat. Mater.*, 2013, **12**, 518–522.
47 G. A. Muller, J. B. Cook, H.-S. Kim, S. H. Tolbert and B. Dunn, *Nano Lett.*, 2015, **15**, 1911–1917.
48 C. Chen, Y. Huang, C. An, H. Zhang, Y. Wang, L. Jiao and H. Yuan, *ChemSusChem*, 2015, **8**, 114–122.
49 X. Liu, G. Xu, H. Xiao, X. Wei and L. Yang, *Electrochim. Acta*, 2017, **236**, 33–42.